TEST RESULTS FROM A LARGE SCALE, HIGH SPEED EDS MAGLEV WHEEL TEST FACILITY

Marc T. Thompson, Ph.D. [1]
Consultant
19 Commonwealth Road
Watertown, MA 02172
(617) 923-1392 *marctt@mit.edu*

Anthony Kondoleon
Charles Stark Draper Laboratory
Cambridge, MA 02139

SUMMARY

The Laboratory for Electromagnetic and Electronic Systems at the Massachusetts Institute of Technology and the Charles Stark Draper Laboratory, for the past few years, have been testing an innovative Electrodynamic Suspension (EDS) system for Maglev applications on their large scale, high speed wheel test facility. Magnetically-levitated high-speed ground transportation technology is a potential solution to increasing highway and air corridor congestion. The Intermodal Surface Transportation Efficiency Act of 1992 (ISTEA) mandated the development of a prototype Maglev demonstration system. **In 1993, a team of MIT, Draper, Bechtel, Hughes Electronics, and** General Motors completed one of four System Concept Definition studies of Maglev systems in the National Maglev Initiative (NMI). This team concept was based on Electrodynamic Levitation and Guidance (EDS) using superconducting magnets and a special arrangement of electrical conductors on the guideway.

The magnetic suspension system was the most important, but least understood part of proposed EDS Maglev systems. Thorough understanding of such systems, with verified analytical design techniques, were essential to formulating improved designs for successful full scale systems. Since the original NMI study, a new "flux-canceling" Maglev geometry has been developed, and the test fixture described in this paper experimentally confirms the predictions and models derived in the course of this study. New design and analytic techniques for Maglev guideway structures have been developed. The test wheel has been successfully run at speeds simulating that of a full-scale Maglev system and resultant data has been taken at speeds significantly higher than the Maglev drag peak.

SYSTEM OVERVIEW

Earlier tests on a similar EDS suspension were done by the MIT/Draper team, with results given in [Kondoleon, et. al.]. During the course of that testing, it was found that the performance of the aluminum guideway conductors was inadequate, due to poor electrical joints, and the results indicated a drag peak above the maximum wheel speed of 1000 RPM. Therefore, a new test wheel was designed with copper conductors. This paper covers the design and test of the 2-meter diameter

[1] Formerly from the Laboratory for Electromagnetic and Electronic Systems, Massachusetts Institute of Technology, Cambridge, MA 02139

wheel, with capability to test at speeds up to 1000 RPM (84 meters/second linear peripheral speed). Two companion papers in these *Proceedings* discuss the development of modeling techniques for EDS Maglev and basic issues related to magnetic control of ride quality, and the history and design detail of the entire project is discussed in the Ph.D. thesis by Marc Thompson.

Iron-Core Levitation Magnet Design

A linearized view of the magnet with copper coils is shown *Fig. 1.* The magnet core is constructed with laser-cut laminations of 0.9 mm thick M19 transformer steel. The core laminations were bonded together with epoxy which was thinned with ketone. The epoxy was thinned so that it would not take up a significant fraction of the core volume. A thin layer of epoxy was sprayed on each lamination. The laminations were then stacked and the structure was pre-cured at 50C for 1 hour. After pre-curing, the structure was then cured at 180 C for 1 hour. The laminations for the pole faces were cut to accommodate a coil bend radius of 1 centimeter to meet a minimum practical radius for a high-temperature superconducting coil. A sample of the lamination stack-up was tested at room temperature, at elevated temperature, and at 77K in a liquid nitrogen bath. There was no damage evident due to differential thermal expansion under repeated testing.

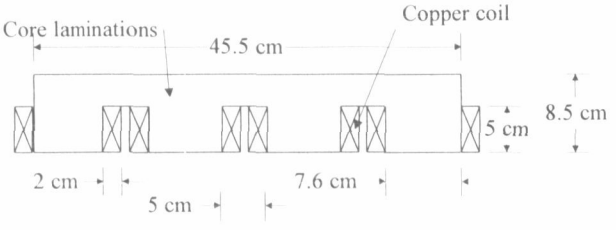

(a) Side view of linearized iron-core magnet with copper coils

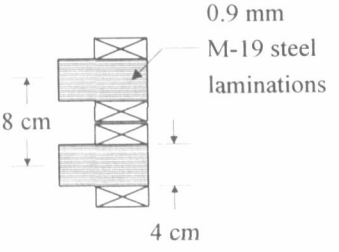

(b) Rear view of dual-row magnet

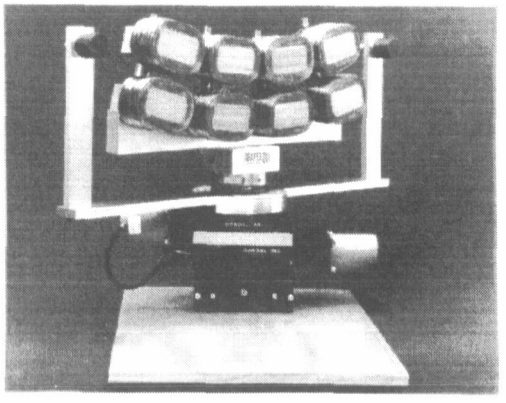

(c) Iron-core magnet, mounted to multi-axis force sensor, showing capacitive position sensors

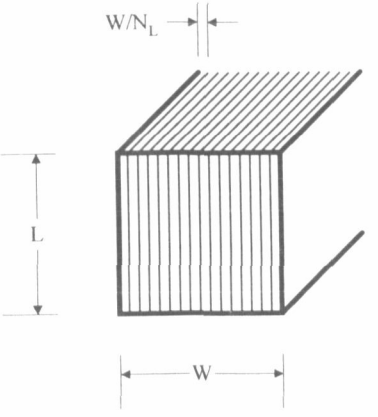

(d) Core laminations

Fig. 1. Detail of magnet design

Eight copper coils were wound with 18 gauge copper magnet wire on an arbor with the same geometry as the magnet polefaces. The final copper coil design had 550 turns in a winding window of 5 cm × 2 cm. The design limit of the copper coils is 8 amps in still air (with current density $J \approx$ 1000 A/cm^2) and 20 Amps when operating in the liquid nitrogen bath ($J \approx 2500$ A/cm^2). The measured resistance of each coil is 3.4 Ω at 300K and 0.442 Ω when cooled to 77K, corresponding to a maximum copper power dissipation per coil of ~200 Watts.

The core laminations were sized by considering the power dissipation per unit length in a section of the core made up of N laminations (*Fig. 1d*) is calculated to be [Zahn]:

$$P \approx \frac{\sigma L W^3 (dB/dt)^2}{16 N_L^2} \qquad [1.]$$

The power loss may be made arbitrarily small by reducing the thickness of the lamination. With a core design with $\sigma \approx 10^6$ (Ωm)$^{-1}$, $N_L = 40$ and expected AC fields of $\Delta B < 0.5$ Tesla at frequencies $f <$ 10 Hz, the power loss in the core is calculated to be less than a Watt.

The magnets were designed so that the top row of coils are operated in a North-South-North-South arrangement (*Fig. 2a*), while the bottom row is offset by one half-cycle. The resultant magnet behaves as a magnetic octapole. A significant advantage of the magnetic octapole is the rapid far-field falloff in the field, which will reduce the shielding required to maintain a low magnetic field in the passenger cabin [Thornton, et. al., 1993].

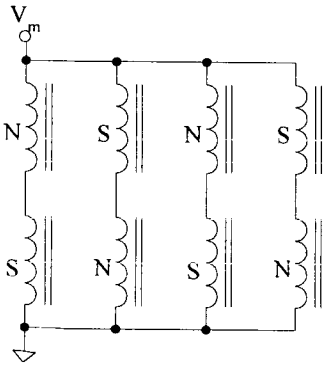

(a) Magnet wiring for flux-canceling Maglev

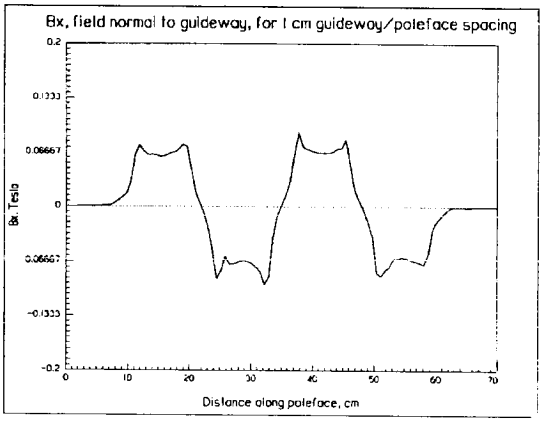

(b) Results of finite element analysis, NI = 2200 Ampere-turns per coil

Fig. 2. Flux-canceling Maglev electrical wiring

Finite element analyses were run on the non-linear iron core design (*Fig. 2b*). The flux density normal to the guideway (B_x) was calculated at a distance $x = 1$ cm from the poleface of the magnet, which is the nominal setpoint for guideway-to-poleface setting. This analysis was checked against measurements taken with a Gaussmeter on the magnet operating with copper coils. The measured value at the center of the poleface was $B_x = 0.069$ Tesla, which matches the calculated value to within a few percent. The finite element analysis was also used to optimize the thickness of the magnet back-iron, so that the weight of the magnet was minimized while insuring that the iron does not saturate for normal operating levels.

Guideway and Test Wheel Mechanical Design

The guideway conductor pattern was constructed from 0.093" thick sheets of 1/2 hard #110 copper. The repeating conductor pattern was cut with an Omax high-pressure numerically-controlled water jet cutter, from 35"×12" sections of copper (*Fig. 3a*) in a 60° section. The water jet cutter has a high-pressure jet 0.030" in diameter and garnet dust is injected into the water stream as an abrasive to increase cutting speed and efficiency. The originally-designed guideway geometry was adjusted to accommodate a minimum cutting line width of 0.030."

The water jet cutting proved to be a more economical method than other methods for copper cutting. The thin slot width does not allow an efficient milling operation. Laser cutting for thick sheets is difficult due to the high thermal conductivity and reflectivity of copper. Wire-EDM is a precision process, but is costly and slow. The water cutting resulted in an acceptable mechanical tolerances of a few thousandths of an inch. Each 60° section took approximately 1 hour to cut. For a production operation, the conductor pattern could be punched out of sheets of copper.

After the individual guideway sections were cut, the inner face of the copper conductor pattern was painted with an electrically-insulating high temperature stove paint. The paint is specified to maintain its integrity to temperatures of 1000 F intermittently, 800F continuous. The 12 guideway sections were then screwed together with brass, round-head #2-58 screws (*Fig. 3b*) spaced approximately 5 inches apart along the outer and inner rim edges. The resulting ring of copper conductors was brazed along the inner and outer diameters, using a 50% lap joint for additional shear strength. The edge of each section was beveled approximately 0.030" so that the solder joint would have higher strength to withstand the shear force due to hoop tension. After the soldering operation, the heads of the screws were ground off.

A silver bearing solder (94% tin, 6% silver) was used for the braze joint. The solder has high strength and a relatively low melting temperature of 535 °F and a yield strength approximately 3 times higher than low cost lead/tin solder. This solder was chosen over a higher-temperature silver-bearing braze joint (where the melting temperature is ~1000-1500 °F) as the lower temperature results in significantly less thermal stress on the copper conductors during assembly.

After brazing, the eccentricity of the copper ring was measured, and found to be true within 1/16 of an inch. A precision mold was constructed, and a composite disk of fiberglass cloth and epoxy 5/8" thick was constructed over the copper conductors with the conductors near one surface of the disk. A step in the fiberglass disk construction process is shown in *Fig. 3c*, with the finished test wheel shown mounted and ready for operation in *Fig. 3d*. A transparent coating of epoxy was used on the front face of the wheel so that the copper conductor pattern is visible.

Test Wheel Safety Testing

The wheel resonant frequencies were calculated so that vibration may be monitored during wheel operation. During wheel acceleration, or if there is a static or dynamic unbalance, wheel resonances will be excited. This analysis is for purposes of calculating first-order resonant frequencies only. In order to calculate various wheel resonant frequencies (or "critical speeds"), a lumped-parameter model was used to calculate the lowest natural frequencies for several different vibration modes. During wheel operation, wheel resonances were monitored using an accelerometer.

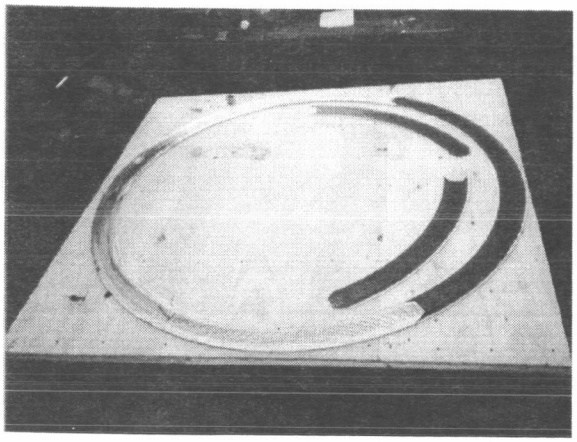

(a) Copper sections coated with non-conductive paint and aligned

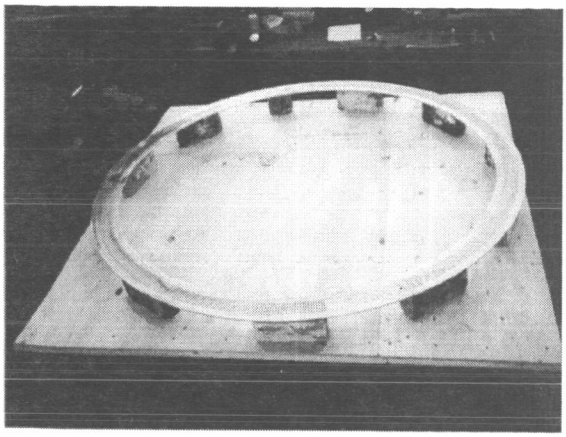

(b) Sections bolted and aligned and ready for brazing

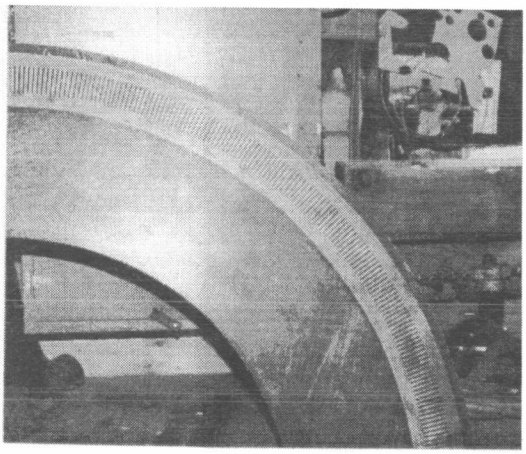

(c) Conductors embedded in fiberglass rim. This is the final seep prior to bolt-hole drilling of the disk and alignment with aluminum hub.

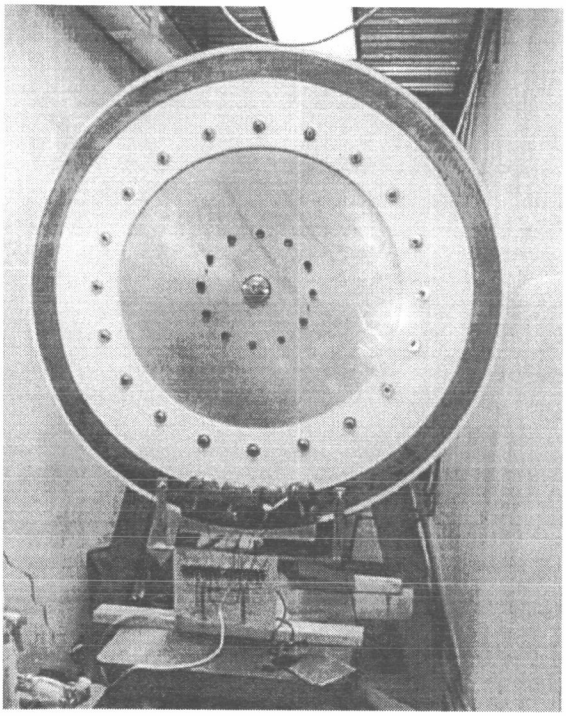

(d) Completed test wheel ready for operation

Fig. 3. Steps in Maglev test wheel construction

Bending and torsional resonances due to the stresses in the aluminum axle were calculated by using standard beam bending and torsion approximations [Den Hartog]. For disk flexure, a vibration mode when the disk itself deforms similarly to the vibration of a drum head, the frequencies of vibration may be found by assuming that the disk behaves as a circular plate (*Fig. 4*) [Blevins, pp. 240] with appropriate boundary conditions. For a disk with a free outer edge, the resonant frequencies are given by:

$$f_{ij} = \frac{\lambda_{ij}^2}{2\pi a^2}\sqrt{\frac{Et^3}{12\gamma(1-\nu^2)}} \qquad [2.]$$

where a is the radius of the disk, E is the Young's modulus of the material in the disk, t is disk thickness, γ is mass per unit area of disk, and ν is the Poisson's ratio. The 3 lowest natural frequencies are found from $\lambda_{ij}^2 = 5.253$, 9.084 and 12.23. The constants λ_{ij}^2 depend on the natural mode shape of interest.

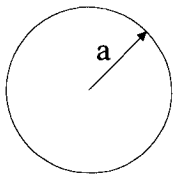

Fig. 4. Circular plate geometry for calculation of flexural resonant modes

This calculation assumes that the disk is of homogeneous material and of constant thickness and is freely supported. The test wheel as built is comprised of fiberglass, copper, and aluminum of varying thickness and is supported by the 3" diameter aluminum axle. In order to calculate resonant modes for disk flexure, average values were used for disk thickness, density, Young's modulus, and Poisson's ratio with calculated results for disk flexure modes (*Table 1*) surprisingly close to the measurements made with accelerometers. The torsional mode may be excited during normal wheel operation at speeds near 230 RPM, but was not noticed during normal operation. Disk flexure modes should not be excited as they are at frequencies higher than the maximum equivalent test wheel operating frequency.

Table 1. Test wheel resonant frequencies

Resonance	***Calculated mode***	***Measured***	***Wheel speed (RPM)***
Torsional	3.85 Hz	---	231
Bending	76.3	---	4580
Disk flexure modes	29.6 Hz, 51, 69	21.9 Hz, 50, 69	1314, 2976, 4116

Air Bearing Design

The air bearing allows low friction, one degree-of-freedom motion of the magnet in the vertical direction. The bearing is under load due to magnetic guidance and drag forces. The bearing allows free motion of the magnet assembly vertically, while constraining the magnet in the other 5 degrees-of-freedom. Further details of the air bearing theory and construction are discussed in [Chiu].

The bearing housings are designed to slide on an alumina shaft 4"×1.36"×30" (10cm×3.5cm×76cm). Before assembly, the alumina shafts were cleaned with sulfuric acid. The air supply was cleaned and dried with a Wilkerson Model X06 desiccant dryer and an ARO 129121-400 Filter/Regulator Unit The bearings are designed to operate with a nominal air gap of 5-15 μm (0.2-0.6 mils). After initial assembly it was found that the main bearing would ground out with torque about the vertical axis of ~ 6 Newton-meters. A secondary outrigger bearing was added to compensate for this torque. Test data shows good performance when the bearing is operated at an air pressure of 140 P.S.I. with z torques up to 16 N-m, with resultant damping of less than 1%. The maximum torque during normal test wheel operation is approximately 25 N-m, so steps were taken to increase the

torque load-bearing capability. With preloading, the load bearing capability of the bearing can be doubled. The air bearing was then tested and it was found that the damping ratio was low, approximately 1% *(Fig. 5d)*.

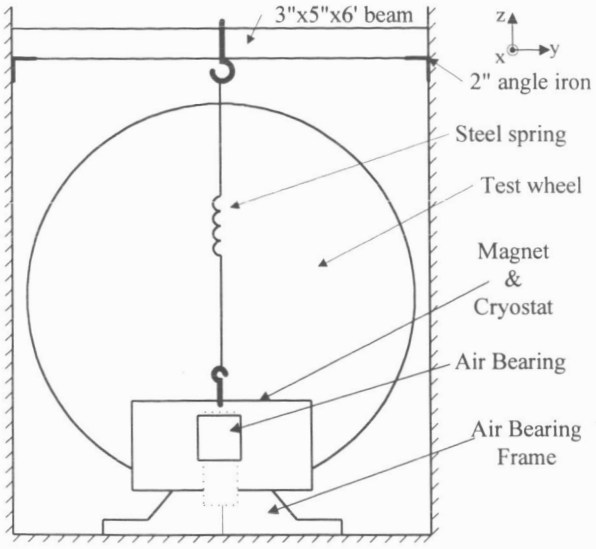

(a) Air bearing schematic view

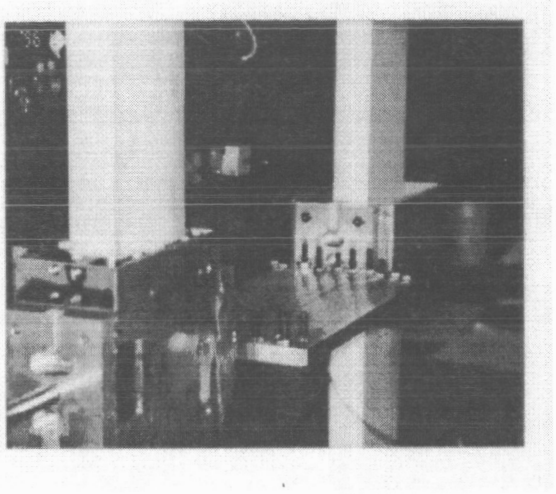

(b) Main and outrigger air bearings, shown sliding on alumina shafts

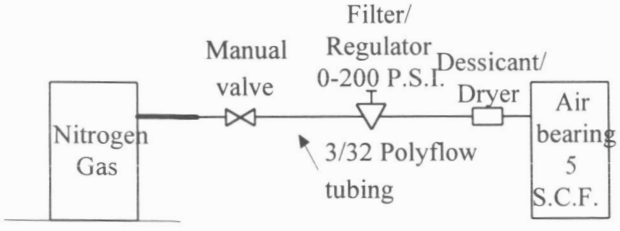

(c) Details of air bearing piping

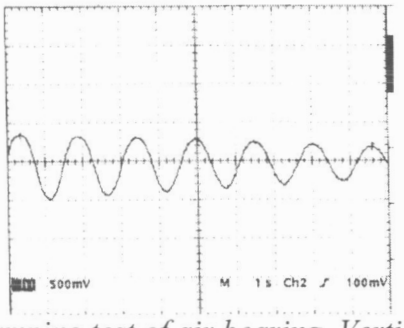

(d) Damping test of air bearing. Vertical 1 cm/division. Oscillation due to steel spring is at approximately 0.6 Hz

Fig. 5. Magnet and air bearing setup

Prototype Superconducting Coil Design and Testing

High-temperature superconducting coils were designed which may be used to retrofit the existing magnet. Several prototype pancake coils were constructed from Bi-2223 superconductor, with HTSC tape dimensions as show in *Table 2* [Haldar]. The cross sectional area of the tape is $A_t = 7.4\times10^{-7}$ m^2, and the area of the superconductor is $A_{sc} = 1.8\times10^{-7}$ m^2, or 25% of the total area. In between each turns of the coil, there is an insulator made of polyimide tape (Kapton) 0.0027" (76 μm) in thickness. After winding and before epoxy impregnation, the edges of the Kapton tape were trimmed off with a razor. A winding width of 1 cm was designed (*Fig. 7a*). Ideally, this would

accommodate $N = 36$ turns per pancake, but due to the bulging of the winding $N = 30$ was wound per coil. After winding, the coil was impregnated with Stycast 2850-GT low-temperature epoxy. The coil was cured at 70 °C for 24 hours.

Table 2. High temperature superconducting tape specification[2]

Tape width	$2a = 3.7$ mm
Tape thickness	$t = 0.2$ mm
I_c at 77K, zero field	11.2 A[3]
Total superconductor area	1.8×10^{-7} m^2
% superconductor	25%
J_c at 77K	6200 A/cm^2
J_{eng} at 77K	1550 A/cm^2
Maximum tensile strain	0.2 %
Maximum bending strain	0.4%

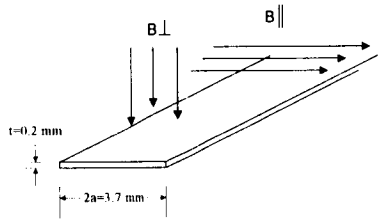

(a) Definition of perpendicular and parallel fields

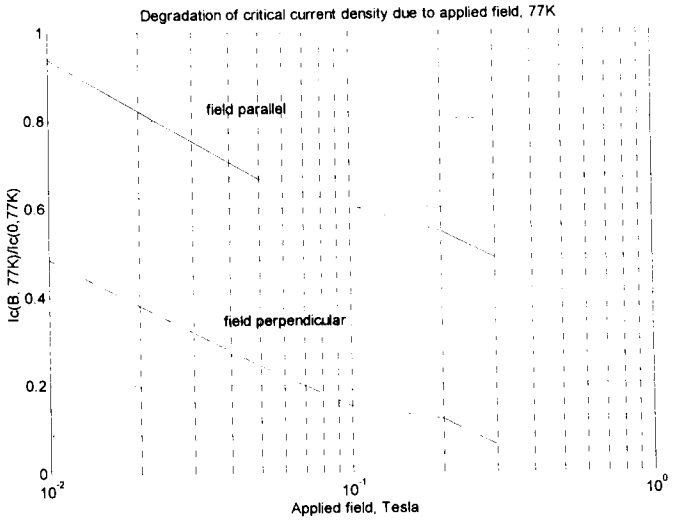

(b) Data from IGC BSCCO-2223 tape [Haldar]

Fig. 6. Degradation of I_c as a function of applied field orientation for HTSC tape

An approximate value for the self-inductance of each pancake coil can be found by using an expression for the inductance of a rectangle of rectangular wire is [Terman, pp. 53]:

$$L = 0.92N^2\left\{(s_1+s_2)\log_{10}\left(\frac{2s_1s_2}{w+t}\right) - s_1\log_{10}(s_1+g) - s_2\log_{10}(s_2+g)\right\} + 0.4N^2\left\{2g - \frac{s_1+s_2}{2} + 0.447(w+t)\right\} \qquad [3.]$$

where L is in microHenries, N is the number of turns in the rectangular coil, s_1 and s_2 are the mean outer lengths of the rectangle side (in meters), w is the width of the rectangle cross section, t is the

[2] Data from Intermagnetics General Corporation

[3] At the time of this writing, tapes with $I_c = 40$A at 77K, 0T are available [Iwasa]

thickness of the rectangle cross section, and g is the diagonal length of the coil cross-section. This model shows good agreement with finite-element analysis and measurements on the prototype coil (*Table 3*).

An I/V curve was generated for the prototype pancake coil (*Fig. 7b*). Results show that the critical current of the coil was degraded by approximately 50% during the winding process, perhaps due to the crude solder connections or the 2 centimeter bend radius[4]. With a tape thickness $t = 0.2$ mm and a minimum bend radius of $\rho = 2$ cm a maximum bending strain of $\varepsilon = t/2\rho = 0.5\%$ is predicted, which is sufficient to degrade the critical current density [Haldar]. However, the coil performs better than a copper coil of identical geometry up to approximately 17 Amperes. For operation as a Maglev magnet coil, the anisotropy of the tape with regard to degradation of critical current due to perpendicular fields makes it advantageous to keep the HTSC material from the poleface area where leakage flux is of the greatest magnitude.

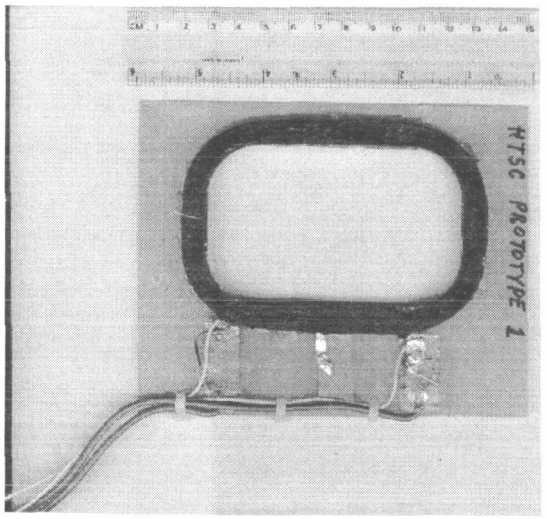

(a) Prototype HTSC coil, mounted and strain-relieved. Shown are large current wires and voltage taps for voltage sensing.

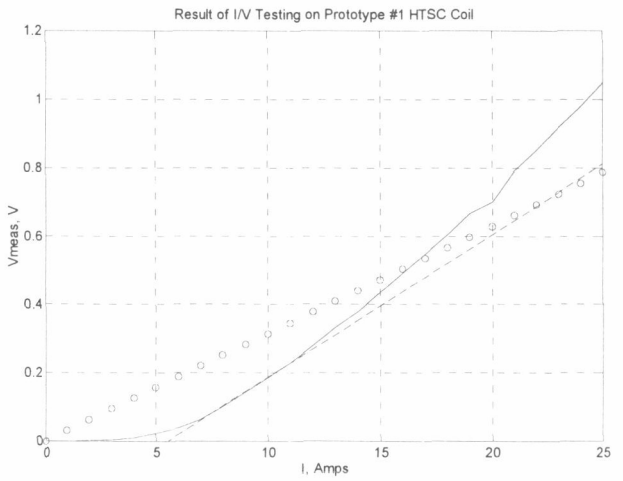

(b) Results of I/V testing with prototype coil, 77K, zero field. Horizontal axis: coil current; Vertical axis: measured voltage at current taps. Solid line --- measurements. Dotted line, prediction, based on $I_c = 5.5$ Amps. ooo --- Comparison with copper coil of same geometry

Fig. 7. Prototype HTSC coil

Table 3. Prototype HTSC coil electrical parameters

	Calculated	***Finite Element Analysis***	***Measurement @ 1 kHz***
R @ 300K	0.3206 Ω	---	0.47 Ω
R @ 77K (when normal)	0.0641 Ω	---	---
L	167 μH	166 μH	155 μH

[4] In this measurement, the actual critical current density if the 10 μV/cm criterion is used is approximately 2 Amperes.

Cryostat and Liquid Nitrogen Delivery System

The cryostat (*Fig. 8)* was designed to hold the iron-core magnet in a liquid nitrogen bath. Level sensors were installed in the cryostat so a nitrogen delivery system can maintain a constant level of coolant over the magnets. The vessel was constructed from sheets of 1/8" thick G-10 fiberglass/epoxy composite, with the corner seams sealed with 2" wide strips of fiberglass boat tape and Emerson and Cuming Stycast™ 2850-GT epoxy. 5 outer walls of the cryostat were insulated with 1" thick Styrofoam. The front face of the cryostat, where the magnetic polefaces are flush, was milled out to a 1/16" thickness, with the magnet polefaces fitting into the groove. The necessary tight spacing between the magnet pole faces and the test wheel did not allow insulation on this face. The aluminum support braces keep the front face of the vessel flush when differential thermal expansion occurs. An outer layer of 1/16" phenolic on 5 faces of the vessel protects the Styrofoam insulation from damage.

The capacity of the cryostat is approximately 8 liters of liquid nitrogen. The latent heat of evaporation of nitrogen at 77 K is $h_L = 161$ J/cm^3. The total cooling requirement includes heat leak from the cryostat and power dissipation from the copper coils. Heat flux leak through the G-10 and Styrofoam insulation was calculated to be $q_{leak,cond.} \approx 150$ W/m^2, corresponding to a heat leak due to conduction of approximately 30 Watts. Radiative heat transfer is a few Watts. The fill rate was measured with the magnets not operating, and was approximately 0.8 liters/hour corresponding to a cryostat heat leak of ~35 Watts. A liquid nitrogen delivery system was designed to maintain a constant level of liquid nitrogen in the cryostat under all operating conditions.

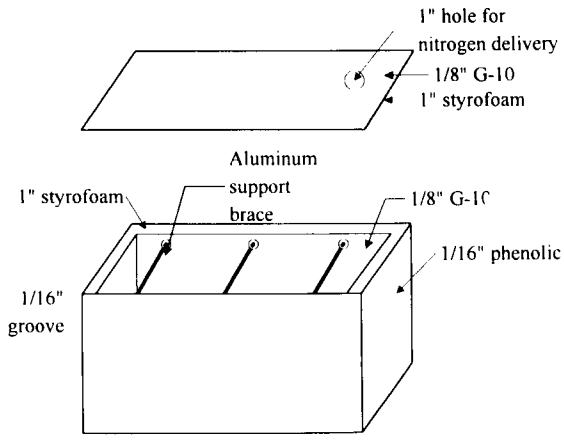

Fig. 8. Cryostat

Test Wheel Speed Control and Data Acquisition System

The data acquisition and test wheel control system (*Fig. 9*) is a computerized station for real time acquisition, processing, display, and storage of sensor data during tests in the facility. The system is comprised of a Macintosh IIfx data acquisition computer, electronics console, motor controllers, specialized software and external sensors. Key parameters are monitored during tests in the facility. Summary data is recorded in the form of plots and spreadsheet compatible data files. Sensors include the multi-axis force sensor to measure forces and torques acting upon the test article, gap sensors to measure the coil to wheel gap, rotation sensors to measure wheel speed, and temperature sensors to measure shaft bearing temperature. The data acquisition and control computer contains 8M RAM and a 240M hard drive, a National Instruments NB-MIO-16 analog/digital

interface card with 16 multiplexed channels of analog input, 8 bits of digital I/O, and 3 counter/timers. Four analog channels are used to acquire gap and temperature sensor data, eight channels have been allocated for coil current measurement and two of the counters for measuring wheel speed. The computer also has two serial ports. One of these is used for communicating with the digital interface of the multi axis force sensor using RS-232 protocol, while the other port is connected to the main motor controller.

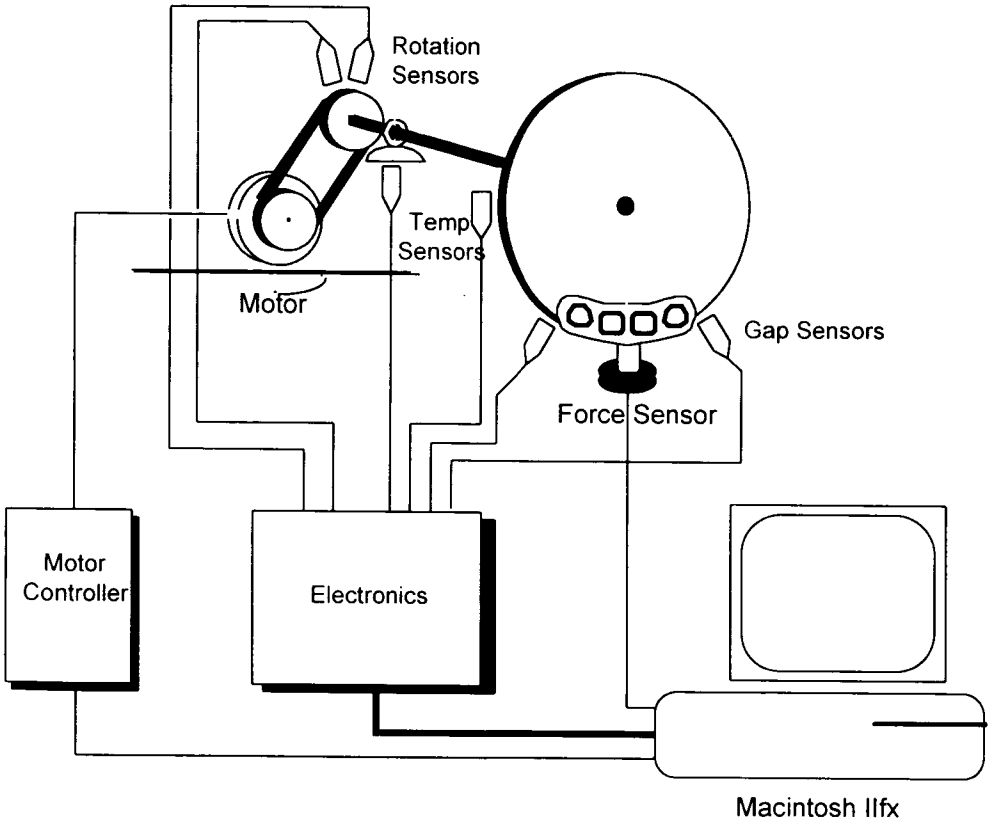

Fig. 9. Data acquisition system and test wheel speed control

TEST RESULTS

Maglev Force Measurements using Force Sensor

The initial testing was done with the magnet mounted to a 6 degree-of-freedom force sensor. The procedure for making basic measurements of forces and moments was as follows:

- The magnet was positioned near the test wheel in the desired vertical (z) and horizontal (x) positions.
- The test wheel was run at the speed corresponding to the desired linear velocity.
- The data acquisition system was activated, beginning a 4 second sampling of force and torque data from the force sensor.
- In the middle of the sampling period, the power supply driving the coils was turned on, and the resulting force transient was measured (*Fig. 10a,b*).

By doing multiple force measurements at different vertical magnet positions and test wheel speeds, Maglev lift (z force), drag (y), and guidance force (x) profiles were calculated (*Fig. 10c,d*) based on the data from the wheel tests. A companion paper in these proceedings describes a model which predicts the lift and drag force profiles with good results.

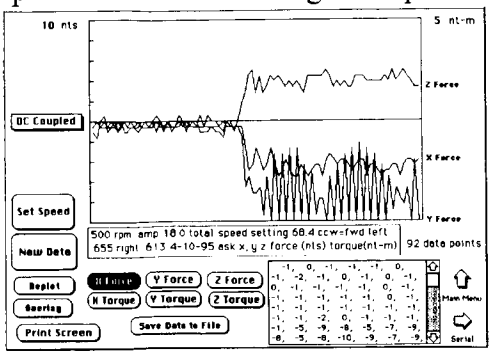

(a) Data acquisition screen showing x force (guidance), y force (drag) and z force (levitation)

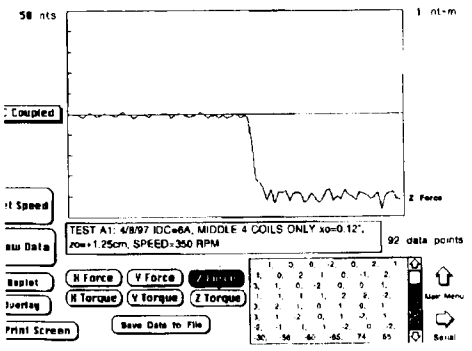

(b) Magnetic lift measurement, showing approximately -50 Newtons of lift at 350 RPM

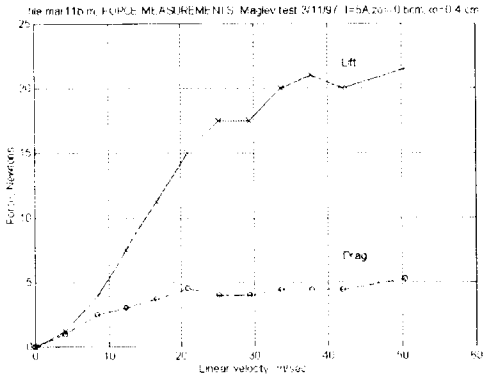

(c) Magnet below null position at z = -0.4 cm

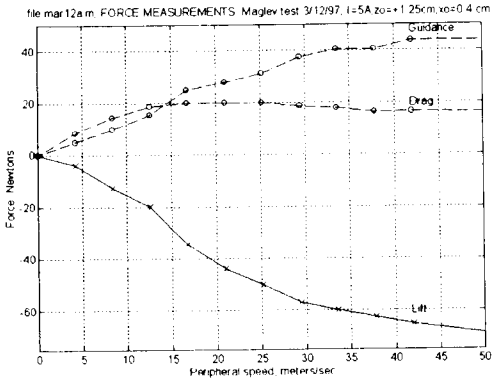

(d) Magnet above null position at z = 1.45 cm

Fig. 10. Lift, drag, and guidance force measurements at different vertical (z) displacements

Vertical Dynamic Tests using Air Bearing and Active Vertical Position Control

In order to test the concept of varying the lift force by using differential current control, a control current source was connected as in *Fig. 11a*. The test wheel was run at 350 RPM. Each of the coils was energized with 6 Amps DC by the main power supply V_m. A 12 Amp peak-to-peak square wave driven by the control current source I_c and the resultant measured lift force is shown *Fig. 11b*. The magnet was set above the null position, and hence the average lift force is negative. This test verifies that it is possible to control the vertical force by controlling the magnet nodes shown in the figure. The advantage of driving at these points is that the effective inductance at the coil terminals is decreased by mutual coupling between magnet coils.

In a follow-up experiment, the air bearing was energized and the magnet was allowed to bounce freely under active current excitation. The DC current for these tests was set to 5 Amperes, the test wheel was set to 350 RPM (30 meters/second peripheral speed), and an underdamped vertical resonant frequency of 1.15 Hz was measured corresponding. In *Fig. 12a*, the differential control terminals are driven with a 12 A p-p, 0.2 Hz current signal. The bottom trace shows little motion, as

the magnet is driven well below the resonant frequency. In *Fig. 12b*, the magnet is driven with a current at 1.1 Hz, near the measured resonant frequency. As expected, there is significant vertical deflection of the magnet.

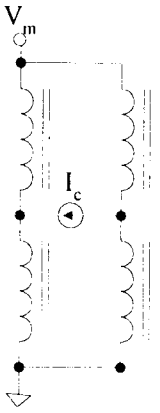

(a) Magnet wiring for differential lift measurement

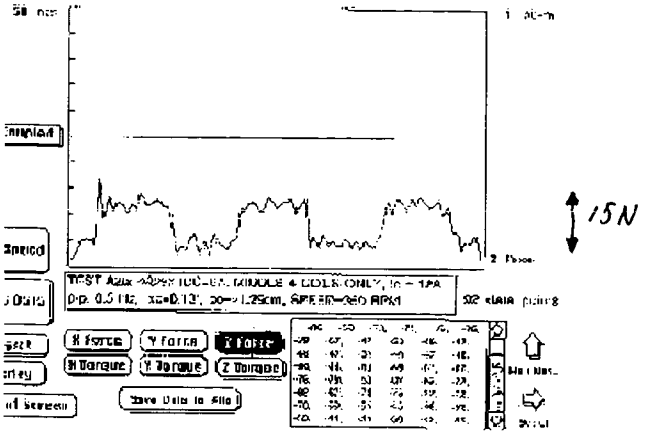

(b) Magnet driven with square wave of control current. Lift force measurement, DC current = 6 Amps/coil, control current = 12 Amp square wave at 0.5 Hz

Fig. 11. Differential lift measurement

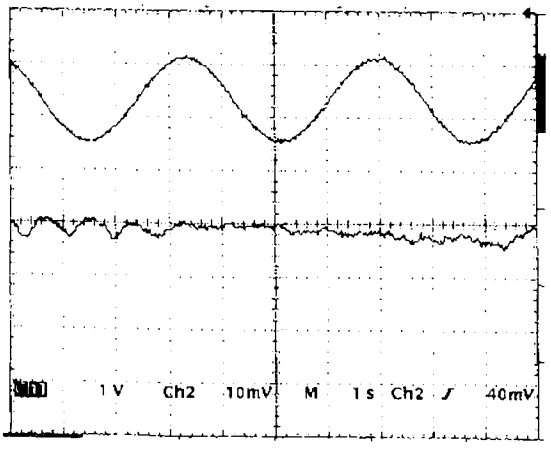

(a) Magnet driven well below resonance Top trace: magnet current, 5 Amps/div. Bottom trace: magnet vertical deflection, 1 cm/div.

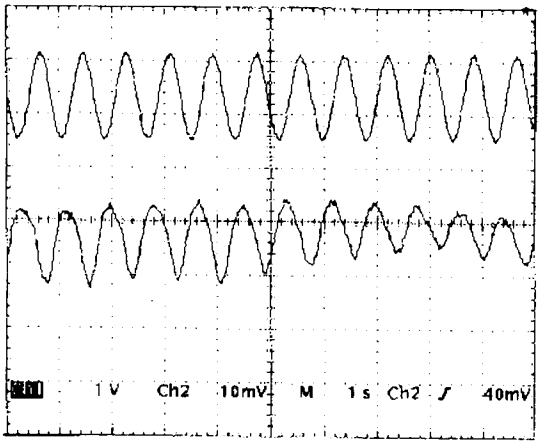

(b) Magnet driven near resonant frequency f = 1.15 Hz. Top trace: magnet current, 5 Amps/div. Bottom trace: magnet vertical deflection, 1 cm/div.

Fig. 12. System driven with sinusoidal current at differential drive terminals

With the air bearing energized and the control system deactivated, the vertical magnet position was perturbed approximately +1 centimeter from the equilibrium position and the resultant transient decay of magnet position was observed (*Fig. 13a*). The oscillatory behavior is at 1.15 Hz with a damping ratio of approximately 1%, corresponding to the expected underdamped EDS response. A similar experiment was run, but with the control system energized with a simple P.I.D.

controller *(Fig. 13b)*. The resultant magnet vertical position response is much more damped ($\varsigma \sim$ 40%) showing that the control system is operating correctly. Further improvement can be made in the transient response by adjusting the loop parameters. This test shows that it is possible to use an active secondary magnetic suspension for ride quality control with this geometry.

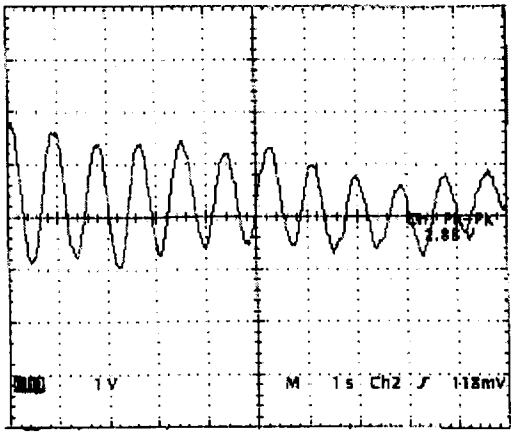

(a) Control system not operating
Initial deflection ~ 1 cm; magnet bounces at EDS natural frequency 1.15 Hz

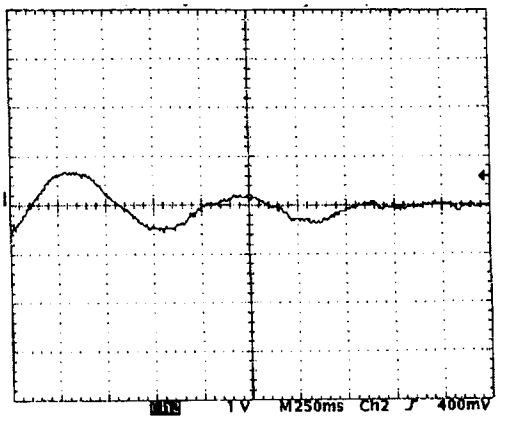

(b) Active damping enabled, using PID controller, damping ratio ~40%. (Note change in time scale)

Fig. 13. Performance of active secondary magnetic suspension

CONCLUSIONS

The successful design and test of a rotating wheel test facility for the study of Maglev electrodynamic suspensions has been demonstrated in this work. The 1/5-scale model suspension described is a starting point for the design of a full-scale, high-efficiency EDS suspension based on high temperature superconducting coils. Development of this model suspension has resulted in improvements and inventions for EDS Maglev, including: the use of an iron core for EDS Maglev, with its associated benefits and costs; verification of operation of the "flux-canceling" topology, including tests of lift force, drag force, and guidance force; use of differential control for controlling vertical forces; AC coil currents for the generation of lift at zero train velocity; use of an active secondary magnetic suspension for ride quality control; and development of scaling laws based on circuit models for the prediction of the performance of a full-scale Maglev system. The test facility operates at linear peripheral speeds exceeding the Maglev drag peak with sufficient safety and mechanical tolerance. At maximum rated test wheel speed, the linear peripheral speed is 84 meters/second, significantly higher than the drag peak velocity. Therefore, both low speed and high speed tests have been done.

Of note is the design of a new low-cost guideway structure which offers good electrical performance. Although much of the guideway conductor design was driven by requirements for high strength to withstand rotating forces, the design could be suitably modified for a full-scale linear guideway where centrifugal force is not an issue. A one degree-of-freedom air bearing was developed which allows low friction vertical motion of the Maglev magnet. The motivation for use of the air bearing was that EDS suspensions are lightly damped and in order to get meaningful test data the mechanical fixturing must have low damping.

Final tests were done using a novel active secondary magnetic suspension. It was shown that it is possible to actively control the magnet position to achieve good ride quality with modest power requirements by using differential current control of the magnets. This opens up the door to the possibility of using HTSC in an active secondary suspension, to take advantage of the robustness of HTSC with regard to AC currents and background fields. These suspension concepts could be further extended to guide the train as it travels down the track by utilizing active horizontal control.

ACKNOWLEDGMENTS

Thanks are due to the U.S. Department of Transportation, Federal Railroad Administration, through the Volpe National Transportation Systems Center, Cambridge, MA, which funded this work, Intermagnetics General Corporation, which provided the superconducting tape used to construct the HTSC coils, Mr. Michael Chiu and Dr. Jeff Roblee who assisted in the design of the air bearing system, and Prof. Richard D. Thornton of the Massachusetts Institute of Technology, who reviewed the work.

REFERENCES

[1] R. D. Blevins, *Formulas for Natural Frequency and Mode Shapes*, R. E. Krieger, Malabar Florida, 1984

[2] M. Chiu, "Low-Cost, Highly-Damped, Precision Linear Motion Using Porous Carbon Air Bearings and Epoxy Replication," Master's Thesis, Massachusetts Institute of Technology, Department of Mechanical Engineering, 1994

[3] J. Den Hartog, *Mechanical Vibrations*, 4th ed., Dover Publications, Inc. New York, 1985

[4] P. Haldar, J. G. Hoehn Jr., J. A. Rice, L. R. Motowidlo, U. Balachandran, C. A. Youngdahl, J. E. Tkaczyk and P. J. Bednarcqyk, "Fabrication and Properties of High-Tc Tapes and Coils Made from Silver-Clad Bi-2223 Superconductors." *IEEE Transactions on Applied Superconductivity*, vol. 3, 1127-30 (1993)

[5] Y. Iwasa, personal communication, 1997

[6] A. Kondoleon, D. Seltzer, R. D. Thornton, and M. T. Thompson, "Development of a Large Scale High Speed Wheel Test Facility," *Proceedings of the Third International Symposium on Magnetic Suspension Technology*, NASA Conference Publication 3336, part 2, pp. 523-534, Dec. 13-15, 1995

[7] F. E. Terman, *Radio Engineers' Handbook*, McGraw-Hill, New York, 1943

[8] M. T. Thompson, "High Temperature Superconducting Magnetic Suspension for Maglev," Ph.D. Thesis, Department of Electrical Engineering and Computer Science, Massachusetts Institute of Technology, May 1997

[9] M. T. Thompson and R. D. Thornton, "Modeling of HTSC-Based Iron Core Flux Canceling Electrodynamic Suspension for Maglev," these *Proceedings*

[10] R. D. Thornton, D. Perreault and T. Clark, "Linear Synchronous Motors for Maglev," *U.S. Dept. of Transportation, Federal Railroad Administration Report DOT/FRA/NMI-92/13*, January 1993

[11] R. D. Thornton and M. T. Thompson, "Magnetically Based Ride Quality Control for an Electrodynamic Maglev Suspension," these *Proceedings*

[12] M. Zahn, *Electromagnetic Field Theory: A Problem Solving Approach*, Krieger Publishing Company, Malabar Florida, 1987